

Indications of a shallow potential in $^{48}\text{Ca}+^{96}\text{Zr}$ fusion reactions

H. Esbensen and C. L. Jiang¹

¹*Physics Division, Argonne National Laboratory, Argonne, Illinois 60439*

(Dated: June 12, 2009)

Fusion data for $^{48}\text{Ca}+^{96}\text{Zr}$ are analyzed by coupled-channels calculations. Puzzling features of a previous analysis are eliminated by applying a potential that has a shallow pocket in the entrance channel. Thus the observed S factor for fusion, which develops a maximum at low energy, can be reproduced fairly well. The high-energy data can also be accounted for but that requires the use of a weak, short-ranged imaginary potential that absorbs the incoming flux near the location of the minimum of the potential pocket. Predictions of the fusion hindrance in other Ca+Zr systems are made and are compared with the systematics that has been developed previously.

PACS numbers: 24.10.Eq, 25.60.Pj

INTRODUCTION

In the field of heavy-ion fusion reactions two major issues have been discussed in recent years. One issue is how to explain the hindrance of fusion at low energies, that is the steep falloff of the measured fusion cross sections, which has been observed in many heavy-ion systems at energies far below the Coulomb barrier (see Ref. [1] and references therein.) The hindrance is often so strong that the S factor for fusion develops a maximum at low energy, and it has been a challenge to reproduce this behavior in coupled-channels calculations. The other issue is the suppression of high-energy fusion data, which is observed when the data are compared to conventional one-dimensional or coupled-channels calculations [2].

A practical solution to the problems mentioned above has been to adjust the parameters of the Woods-Saxon shaped, ion-ion potential that is used in the calculations. Thus it has been realized that by using a large diffuseness (in combination with a deep potential and a small radius parameter) one can often resolve the problem of a suppression at high energy [2]. However, the diffuseness that is required to reproduce the high-energy data, for example, in the fusion of $^{16}\text{O}+^{208}\text{Pb}$, is different from the value that is needed to fit the low-energy data [3]. Moreover, the values are often unrealistic and much larger than the empirical diffuseness which has been extracted from analyses of elastic scattering data or obtained from double-folding potentials [4]. It has recently been shown that a large diffuseness is also inconsistent with quasi-elastic scattering data [5].

A good example on a system where both of the above mentioned problems exist is the fusion data for $^{48}\text{Ca}+^{96}\text{Zr}$ [6]. The problems were solved in the original analysis of the data by using a large diffuseness, $a = 0.85$ fm, instead of the empirical value, $a = 0.677$ fm (Eq. (III.44) of Ref. [4]). The measurements [6] were later supplemented with two new low-energy data points [7] and they confirmed that the S factor for this system does develop a maximum at low energy.

Instead of using an ion-ion potential with an anoma-

lously large diffuseness, the double-folding technique is applied to construct an ion-ion potential which has a realistic behavior at large distances and is adjusted at small distances between the reacting nuclei to produce a shallow pocket in the entrance channel potential [8]. The potential used is the so-called M3Y+repulsion potential and the construction of it is described in Ref. [8]. The basic feature of this potential is that the existence of a shallow pocket in the entrance channel makes it possible to explain the steep falloff of the fusion data at low energies, and it also helps explaining the measured fusion cross sections at high energies [8, 9, 10]. However, in order to reproduce the high-energy data, it is often necessary to include a short-ranged, imaginary potential in the calculations of the cross sections [9, 10].

The M3Y+repulsion potential is applied in coupled-channels calculations of the fusion cross section for $^{48}\text{Ca}+^{96}\text{Zr}$. The purpose is to demonstrate that the energy dependence of the measured S factor for fusion can be reproduced at low energies by employing this potential. It is also shown that the calculated cross sections at high energies are sensitive to the nuclear potential and to the nuclear structure input, and it is possible to reproduce the high-energy data by using a realistic structure input and employing the M3Y+repulsion potential, in combination with a short-ranged imaginary potential.

Finally, the hindrance in the fusion of other Ca+Zr isotopes at low energies is discussed and compared with the systematics we have developed previously [1], and predictions are made of the energy where the S factor for fusion is expected to develop a maximum in those cases where it has not yet been observed experimentally.

ION-ION POTENTIAL

The construction of the double-folding ion-ion potential for $^{48}\text{Ca}+^{96}\text{Zr}$ is based on the effective M3Y interaction which is supplemented with a contact term for the exchange part [8]. The densities are parametrized as fermi functions with the radius 3.675 fm and diffuseness

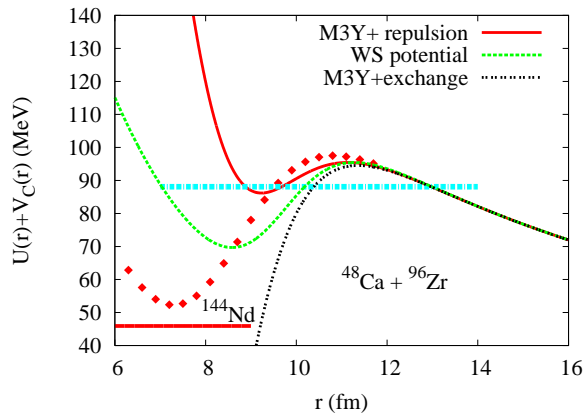


FIG. 1: (color online) The M3Y+repulsion potential (red solid curve) is compared to the Woods-Saxon potential (middle dashed curve) and to the pure M3Y+exchange potential (lowest black dashed curve). The diamonds show the potential with large diffuseness that was used in Ref. [6]. The energy of the compound nucleus ^{144}Nd and the energy band where the S factor for fusion has a maximum (≈ 88 MeV) are also indicated.

0.525 fm for ^{48}Ca , and the radius 5.02 fm and diffuseness 0.55 fm for ^{96}Zr . These two densities produce the RMS matter radii of 3.45 and 4.39 fm, respectively, which are consistent with the measured charge radii.

The M3Y double-folding potential (including exchange) is illustrated by the lowest dashed curve in Fig. 1. It is unrealistic at short distances between the two nuclei because it is much deeper than the ground state energy of the compound nucleus. The M3Y interaction has therefore been corrected by supplementing it with a repulsive term as described in Ref. [8]. The densities that are used in calculating the associated repulsive, double-folding potential have a sharper profile, with the diffuseness $a_{\text{rep}}=0.4$ fm, but the radii are the same as used above to calculate the ordinary M3Y double-folding potential. The strength of the repulsive contact term, $V_{\text{rep}} = 507$ MeV, was adjusted to produce the nuclear incompressibility $K = 223$ MeV.

The entrance channel potential for the M3Y+repulsion potential is illustrated by the upper solid curve in Fig. 1. It has a rather shallow pocket inside the Coulomb barrier. Also shown is the entrance channel potential obtained from a Woods-Saxon (WS) potential, which is similar to the empirical Akyüz-Winther potential [4]. The slightly adjusted parameters of this WS potential are $V_0 = -77.18$ MeV, $R = 9.686$ fm, and $a = 0.677$ fm. They produce the same Coulomb barrier height, $V_{CB} = 95.4$ MeV, as the M3Y+repulsion potential but the pocket is deeper. The fusion cross sections obtained in the coupled-channels calculations that are based on these two potentials are essentially the same at energies close to the Coulomb barrier but differ at energies far below the Coulomb barrier. This will be discussed in the next section.

TABLE I: Structure input for ^{48}Ca [11] and ^{96}Zr [12].

Nucleus	λ^π	E_x (MeV)	β_λ^C	σ_λ^C (fm)	σ_λ^N (fm)
^{48}Ca	2^+	3.832	0.102	0.126	0.190
	$2\text{PH}(2^+)$	4.297	0.082	0.101	0.101
	3^-	4.507	0.203	0.250	0.190
^{96}Zr	2^+	1.751	0.079	0.123	0.123
	3^-	1.897	0.295	0.457	0.457

The entrance channel potential which was used in Ref. [6] (with diffuseness $a = 0.85$ fm) is indicated by the diamonds in Fig. 1. This potential is deeper than the other two potentials mentioned above but none of them are deeper than the ground state energy of the compound nucleus ^{144}Nd , which is indicated by the lowest horizontal line. The broad horizontal band near 88 MeV indicates the energy where the experimental S factor for fusion develops a maximum.

COUPLED-CHANNELS CALCULATIONS

The nuclear structure input to the coupled-channels calculations associated with the excitation of the 2^+ and 3^- states in projectile and target is shown in Table I. The calculations include all one-phonon, two-phonon, and mutual excitations of these one-phonon excitations. That is a total of 15 channels in the rotating frame approximation [8]. The coupling between the one- and two-phonon states is assumed to be vibrational (harmonic), except for the quadrupole excitation of ^{48}Ca for which we use a weaker one- to two-phonon coupling strength (see Table I) which is based on the known $0_2^+ \rightarrow 2_1^+$ transition strength [12].

The conventional assumption $\beta^N = \beta^C$ does not work so well for ^{48}Ca . The empirical nuclear coupling strengths that will be used are shown in the last column of Table I. They are expressed in terms of the values of

$$\sigma_\lambda^N = \frac{\beta_\lambda^N R_N}{\sqrt{4\pi}}, \quad (1)$$

and were determined by analyzing measurements of the inelastic scattering of ^{16}O on ^{48}Ca [11].

The fusion cross sections are determined by imposing ingoing-wave boundary conditions at the position of the minimum of pocket in the entrance potential. The results of coupled-channels calculations are compared in Fig. 2 to the data of Refs. [6, 7]. The top dashed (green) curve is based on the empirical Woods-Saxon potential discussed in the previous section. It is seen to reproduce the data quite well, except at the very lowest energy. The overall χ^2/N (based on statistical errors only) is about 4 for this calculation.

The solid (red) curve in Fig. 2 is the coupled-channels result obtained with the M3Y+repulsion potential. It

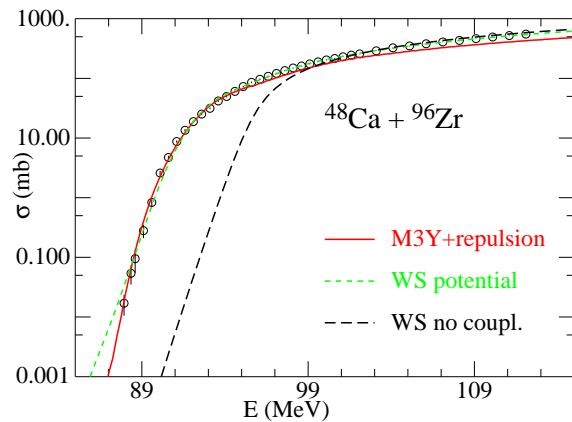


FIG. 2: (color online) Measured fusion cross sections for $^{48}\text{Ca} + ^{96}\text{Zr}$ [6, 7] are compared to coupled-channels calculations based on the Woods-Saxon (WS, green dashed curve) and M3Y+repulsion (red solid curve) potentials. The lowest dashed (black) curve is the no-coupling limit for the WS potential.

reproduces the data very well at low energies but is below the data at high energies. The latter problem can be solved as mentioned earlier by employing short-ranged imaginary potential. The explicit form used below is

$$W(r) = \frac{-10 \text{ MeV}}{1 + \exp((r - r_p)/a_w)}. \quad (2)$$

where r_p is the radial distance between the reacting nuclei at the minimum of the pocket, and the diffuseness a_w is set to 0.2 fm. The effect of the imaginary potential, Eq. (2), is illustrated below (see Fig. 5.)

Barrier distribution

The effect of couplings on the calculated fusion cross section is very strong. This can be seen by comparing the coupled-channels calculations to the no-coupling limit which is shown by the lower dashed curve in Fig. 2. The effect is to shift the calculated cross section by roughly 4–5 MeV to lower energies.

The couplings produce some interesting features in the barrier distribution for fusion [13], which is defined as the second derivative of the energy-weighted fusion cross section with respect to the center-of-mass energy E ,

$$B(E) = \frac{d^2(E\sigma_f)}{dE^2}. \quad (3)$$

The barrier distributions, which are shown in Fig. 3, were calculated by the finite difference method using the same energy step $\Delta E = 2$ MeV that was used in the earlier work [6]. The measured distribution is broad and contains several peak structures. The red solid curve in Fig. 3 is the distribution derived from the coupled-channels

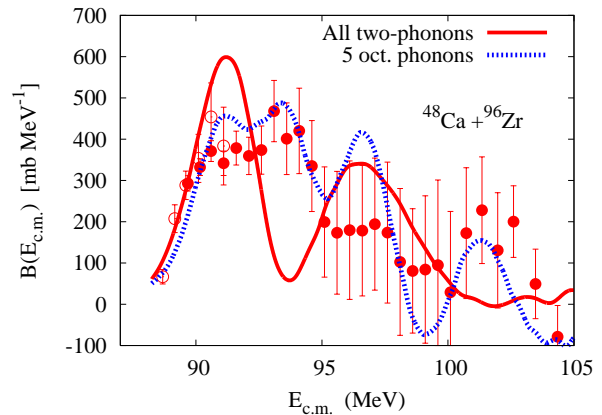


FIG. 3: (color online) Barrier distributions obtained from the fusion cross sections shown in Fig. 2 using $\Delta E = 2$ MeV (open circles for $\Delta E = 1$ MeV). The red solid curve was derived from the M3Y+repulsion calculation shown in Fig. 2. The blue, dashed curve was obtained from a calculation that includes up to 5 phonons of the octupole excitation in ^{96}Zr .

calculations that are based on the M3Y+repulsion potential. It is broad and consists of two strong peaks but the shape is not in good agreement with the data.

It was demonstrated in Ref. [6] that some of these peak structures in the measured barrier distribution can be reproduced by including up to three-phonon excitations of the octupole mode in ^{96}Zr . The blue dashed curve in Fig. 3 is the barrier distribution one obtains by considering up to five phonon excitations of the octupole mode in ^{96}Zr in the coupled-channels calculations. The other excitations shown in Table I were not included in these calculations for practical reasons. The shape of the distribution (the blue dashed curve) seems to trace the four peak structures of the measured distribution rather well, and it appears to be in better agreement with the data than the three-phonon calculation presented in Ref. [6]. It is obvious from this comparison that the calculated barrier distribution is very sensitive to multiphonon excitations of the soft octupole mode in ^{96}Zr .

The fusion cross section obtained in the calculation that is based on up to five-phonon octupole excitations has an average deviation of about 10% from the data (i. e., we need a systematic error of 10% in order to obtain a χ^2 per point of 1), whereas the solid curve in Fig. 1 deviates on average by 7%. It is possible that one would be able to improve the overall fit to the data by including more channels in the calculation. However, such a calculation would probably not be very realistic because of the sensitivity to the empirically poorly known multiphonon excitations. The main point we want to make is that the standard calculation, which is based on couplings to one- and two-phonon excitations, provides a reasonable fit to the data and by applying the M3Y+repulsion potential it is possible to reproduce the fusion hindrance observed

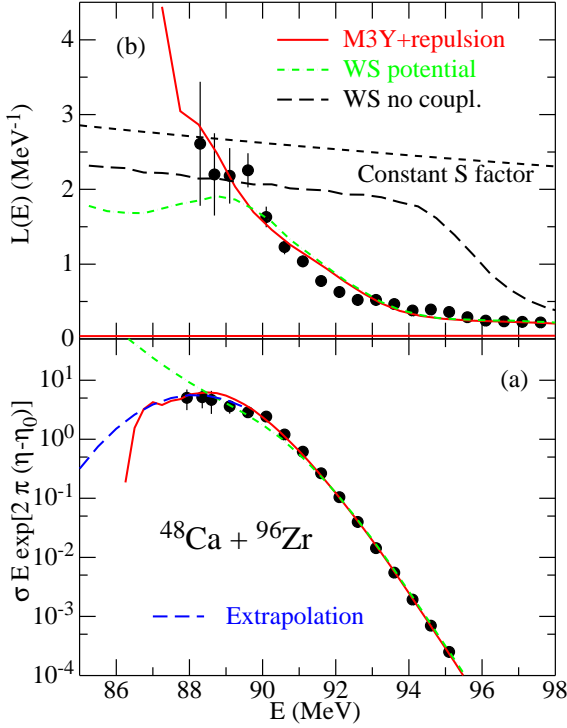


FIG. 4: (color online) (a) The measured S factors for the fusion of $^{48}\text{Ca} + ^{96}\text{Zr}$ [6, 7] are compared to the two coupled-channels calculations shown in Fig. 2. The value of η_0 was set to $\eta_0 = 74.58$. The blue dashed curve is the prediction of Eq. (8) and the parameters of Table II. The logarithmic derivatives, Eq. (5), are shown in (b). The top short-dashed curve is the constant S factor limit, Eq. (6); the long-dashed curve is the no-coupling limit for the WS potential.

at energies far below the Coulomb barrier.

Behavior at low energy

The low-energy behavior of the fusion cross sections is illustrated in Fig. 4a in terms of the S factor for fusion, which is defined by,

$$S(E) = \sigma_f(E) E \exp(2\pi\eta(E)), \quad (4)$$

where E is the center-of-mass energy, $\eta = Z_1 Z_2 e^2 / (\hbar v)$ is the Sommerfeld parameter, and v is the relative velocity. It is seen that the S factor for the coupled-channels calculations that are based on the Woods-Saxon potential keeps increasing with decreasing energy. The calculation based on the M3Y+repulsion potential, on the other hand, develops a maximum before it goes to zero near 86.2 MeV, which is the energy of the pocket minimum for the M3Y+repulsion potential shown in Fig. 1. The calculated fusion cross section must go to zero at this energy because we use a real potential at low energy and use ingoing-wave boundary conditions to determine

the fusion probability.

The coupled-channels calculations that are based on the M3Y+repulsion potential provide the best description of the low-energy S factor data shown in Fig. 4a. In fact, the S factor data have just reached a maximum at the lowest energies, which is a characteristic feature for the onset of the fusion hindrance phenomenon in systems with a negative Q -value for fusion, and this feature is reproduced by using a shallow entrance channel potential. The extrapolation to very low energies, which will be discussed later on, is also shown in the figure. It has a nearly parabolic shape and the lowest data points are seen to fall on the top of this curve.

Another way to illustrate the fusion hindrance is to show the logarithmic derivative of the energy weighted fusion cross section,

$$L(E) = \frac{d \ln(E\sigma_f)}{dE} = \frac{1}{E\sigma_f} \frac{d(E\sigma_f)}{dE}. \quad (5)$$

This quantity is shown in Fig. 4b. The calculations based on the Wood-Saxon potentials are seen to reach a local maximum at low energies. The data and the calculations based on the M3Y+repulsion potential, on the other hand, keep increasing steeply with decreasing energy. They both intersect the upper ‘constant S factor’ line, which is the logarithmic derivative one obtains by assuming a constant S factor [1],

$$L_{cs}(E) = \frac{\pi\eta}{E} = \frac{0.495 Z_1 Z_2 \sqrt{\mu}}{E^{3/2}}. \quad (6)$$

Here $\mu = A_1 A_2 / (A_1 + A_2)$ is the reduced mass number. At the point where $L(E)$ intersects with $L_{cs}(E)$, the associated S factor will have a maximum (see Fig. 4a.)

Behavior at high energy

The behavior of the fusion cross sections at high energies is illustrated in Fig. 5. The lowest dashed curve is the result of the coupled-channels calculation that is based on the M3Y+repulsion potential. This calculation is suppressed compared to the data, as already pointed out in the discussion of Fig. 2. However, the discrepancy with the data can essentially be eliminated by including in the calculation the weak, short-ranged imaginary potential, Eq. 2. This is illustrated by the red solid curve. The result obtained with the Woods-Saxon potential (with diffuseness $a = 0.677$ fm) and the structure input from Table I is shown by the blue dashed curve which is difficult to see because it is essentially identical to the solid curve in Fig. 5. This remarkable feature is the reason why the two calculations give essentially the same quality fit to the data as mentioned earlier.

Good agreement with the high energy data could only be achieved in Ref. [6] by using a large diffuseness in the

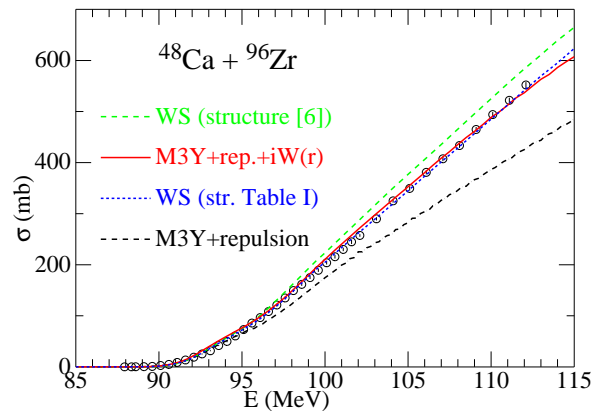


FIG. 5: (color online) Linear plot of the fusion cross sections for $^{48}\text{Ca} + ^{96}\text{Zr}$ [6]. The upper dashed curve is based on the WS potential with diffuseness $a = 0.677$ fm and the structure input from Ref. [6]. The next (blue) dashed curve is based on the same potential but structure input is from Table I. The red solid and the lower dot-dashed curves are the coupled-channels calculations, based on the M3Y+repulsion potential and the structure input of Table I, with and without the effect of the short-ranged imaginary potential $iW(r)$, respectively.

Woods-Saxon potential. This seems to contradict the results discussed above, where the Woods-Saxon potential with ‘normal’ diffuseness provided an excellent description of the high-energy data when applied in coupled-channels calculations. The reason for this apparent contradiction is that the structure input of Table I is different from the structure input used in Ref. [6], in particular for ^{48}Ca . The coupled-channels calculations were therefore repeated using the structure input from Ref. [6] and a Woods-Saxon potential with the ‘normal’ diffuseness $a = 0.677$ fm. The result is shown by the upper dashed curve in Fig. 5. It is seen that the data are suppressed compared to this calculation, in accord with the findings in Ref. [6].

FUSION HINDRANCE IN CA+ZR SYSTEMS

Many fusion reactions involving medium heavy nuclei have been measured at Legnaro. Here we focus on the measurements that have been performed with different isotopes of calcium and zirconium [6, 15, 16]. The purpose is to extract information about the fusion hindrance phenomenon at extreme subbarrier energies and to compare with the results that have been obtained for other systems [1, 17, 18].

The fusion hindrance for systems with negative Q -value can be characterized by the energy E_s where the S factor for fusion has a maximum at low energy [1]. Although many measurements do not reach such low energies, it is still possible to determine E_s by extrapolation of the existing data. It was found that the log-

TABLE II: Parameters for the fusion hindrance behavior, E_s , L_s , A_0 , B_0 and σ_s , obtained for the Ca+Zr systems. The last column is the reference energy E_s^{ref} defined in Eq. (9).

System	E_s MeV	L_s MeV^{-1}	A_0 MeV^{-1}	B_0 $\text{MeV}^{1/2}$	σ_s mb	E_s^{ref} MeV
$^{40}\text{Ca} + ^{90}\text{Zr}$	93.2	2.31	-17.1	4222	0.37	92.8
$^{40}\text{Ca} + ^{94}\text{Zr}$	86.4	2.61	-11.6	3585	3.8E-3	93.2
$^{40}\text{Ca} + ^{96}\text{Zr}$	83.1	2.77	-7.43	2783	3.7E-5	93.4
$^{48}\text{Ca} + ^{90}\text{Zr}$	90.0	2.59	-12.9	3775	0.025	96.7
$^{48}\text{Ca} + ^{96}\text{Zr}$	88.1	2.71	-13.8	4528	0.030	97.4

arithmic derivative of the energy-weighted fusion cross section, the $L(E)$ defined in Eq. (5), has a nearly linear dependence on energy at energies around the S factor maximum [1, 18]. A slightly different (non-linear) parametrization is used in the following [19], namely,

$$L(E) = A_0 + \frac{B_0}{(E + Q)^{N_p}}, \quad (7)$$

where Q is the Q value for the fusion reaction, and we assume that $N_p = 3/2$. This expressions implies that $L(E) \rightarrow \infty$ for $E \rightarrow -Q$ in agreement with the constraint that the cross section must go to zero when the center-of-mass energy E approaches the ground state energy, $-Q$, of the compound nucleus [1, 18].

Once the parameters A_0 and B_0 in Eq. 7 have been determined from the low energy data, it is straightforward to extrapolate and find the energy E_s where $L(E)$ intersects the logarithmic derivative $L_{cs}(E)$ for a constant S factor, Eq. (6). Results for the systems $^{40}\text{Ca} + ^{90,94,96}\text{Zr}$ and $^{48}\text{Ca} + ^{90}\text{Zr}$ using this extrapolation method are shown in Fig. 6a. The parameters obtained by fitting the low-energy $L(E)$ data and the extrapolated values of E_s are collected in Table II. There we also give the value L_s which is the logarithmic derivative at the energy E_s .

The analytic expression for the cross section one obtains from the parametrization (7) of $L(E)$ is,

$$\sigma(E) = \sigma_s \frac{E_s}{E} \exp\left(A_0(E - E_s) - \frac{B_0}{(N_p - 1)(E_s + Q)^{N_p - 1}} \left[\left(\frac{E_s + Q}{E + Q}\right)^{N_p - 1} - 1\right]\right). \quad (8)$$

The only unknown parameter in this expression is the normalization factor σ_s which is the fusion cross section at the energy E_s . It can be obtained by normalizing to the low-energy fusion data and the resulting values are given in Table II. The S factors that have been determined in this way are shown by the curves in Fig. 6b. They have a characteristic, nearly parabolic behavior at low energy. The measured S factors have not reached a maximum for most of these systems but the data for

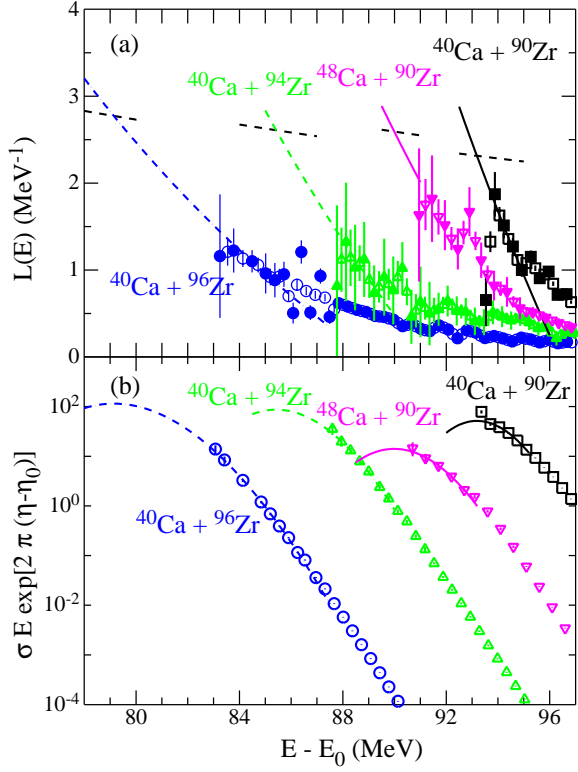


FIG. 6: (color online) Logarithmic derivative (a) and S factors (b) for the fusion of $^{40}\text{Ca}+^{90,94,96}\text{Zr}$ [15, 16] and $^{48}\text{Ca}+^{90}\text{Zr}$ [6]. The curves in (a) are fits to the measured $L(E)$ using the parameterization Eq. (7). The upper, nearly horizontal dashed lines show the constant S factor limit, Eq. (6). The curves in (b) are the S factors predicted by Eq. (8) and the parameters in Table II. The parameters E_0 and η_0 used in the plot are $E_0 = 0, 1, 3, 0$ MeV and $\eta_0 = 68.59, 70.87, 71.71, 73.98$ for the systems $^{40}\text{Ca}+^{90,94,96}\text{Zr}$ and $^{48}\text{Ca}+^{90}\text{Zr}$, respectively.

$^{40}\text{Ca}+^{90}\text{Zr}$ are close (although the lowest point has a somewhat unusual behavior.) The S factor for the system $^{48}\text{Ca}+^{96}\text{Zr}$, which was already shown in Fig. 4a, did reach a maximum at the lowest energy, and the extrapolation obtained from the parameters in Table II was also shown there.

We have previously studied the systematics of the energy E_s for other heavy-ion systems (Refs. [1, 18]) and found that the value of L_s , i. e., the logarithmic derivative of the energy weighted cross section at the energy E_s , has a nearly constant value of $L_s^{\text{ref}} = 2.33 \text{ MeV}^{-1}$ for systems that consist of closed shell nuclei or of nuclei that are relatively stiff. Inserting such a constant value of L_s and the energy E_s into Eq. (6), it is seen that the system dependence of E_s is governed by the entrance channel parameter

$$\zeta = Z_1 Z_2 \sqrt{\mu} = Z_1 Z_2 \sqrt{A_1 A_2 / (A_1 + A_2)}.$$

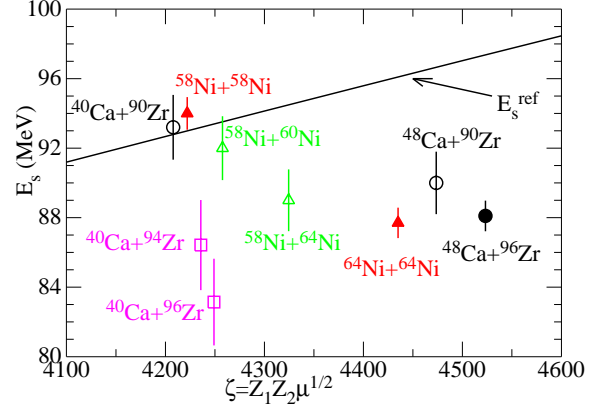


FIG. 7: The energy E_s for Ca+Zr and Ni+Ni systems. The solid curve is the reference value, Eq. (9). The open symbols are extrapolated values. The solid symbols are for systems where a maximum in the S factor has been observed.

The expression one obtains for E_s is the reference energy

$$E_s^{\text{ref}} = (0.495 \zeta / L_s^{\text{ref}})^{2/3} \text{ (MeV)}, \quad (9)$$

which is illustrated by the solid curve in Fig. 7. For systems consisting of soft or open shell nuclei, the value of E_s is usually lower than the reference value E_s^{ref} . The deviation of E_s from E_s^{ref} is a measure of the softness the systems [17, 18, 20].

The values of E_s extracted from the data for the different Ca+Zr systems [6, 7, 15, 16] are shown in Fig. 7. Also shown are the values obtained previously for the Ni+Ni systems, consisting of different nickel isotopes. It is seen that the extrapolated value of E_s for $^{40}\text{Ca}+^{90}\text{Zr}$ falls on the solid line, consistent with the closed shell nature of these two nuclei. The results for the two soft and open shell systems, $^{48}\text{Ca}+^{96}\text{Zr}$ and $^{64}\text{Ni}+^{64}\text{Ni}$, are similar and fall far below the solid curve. The value of E_s for $^{48}\text{Ca}+^{96}\text{Zr}$, for example, is 9.3 MeV below the reference value E_s^{ref} , according to Table II.

The values of E_s are also far below the reference value E_s^{ref} for some of the other Ca+Zr systems. This is partly caused by the softness of the reacting nuclei or by transfer reactions. Stefanini et al. in Ref. [16] pointed out that neutron transfer with positive Q value should affect the fusion of $^{40}\text{Ca}+^{94}\text{Zr}$ and $^{40}\text{Ca}+^{96}\text{Zr}$ and enhance it below the Coulomb barrier. Consequently, the fusion hindrance would be pushed to lower energies.

There is a correlation between the ratio E_s/E_s^{ref} and the number of valence neutrons in the two reacting nuclei, which was first pointed out in Ref. [20] for nickel induced fusion reactions. A similar trend is observed in Fig. 7 for the Ca+Zr systems. In order to see the interplay between neutron transfer with positive Q value and the fusion hindrance behavior, it would be very interesting to measure the fusion of $^{40}\text{Ca}+^{94}\text{Zr}$ and $^{40}\text{Ca}+^{96}\text{Zr}$ down to much smaller cross sections.

CONCLUSIONS

We conclude that there are strong indications of a fusion hindrance at low energy in the data for $^{48}\text{Ca}+^{96}\text{Zr}$. The S factor does reach a maximum at the lowest energies and there is a preference among the coupled-channels calculations presented here for those that are based on a shallow potential in the entrance channel. In this respect, the fusion data exhibit the same characteristics that have been observed in many other heavy-ion systems [1, 8, 9, 10].

The systematics of the fusion hindrance in other Ca+Zr systems, where it has not yet been confirmed experimentally, was discussed and predictions were made of the energy E_s where the S factor for fusion is expected to develop a maximum. This energy can be far below the energy predicted by the empirical formula, which was developed for systems consisting of stiff or closed shell nuclei. The deviation of E_s from the empirical formula seems to correlate with the number of valence neutrons in the reacting nuclei, which may reflect an increased softness or a stronger effect of neutron transfer.

The behavior of the high-energy fusion data can also be reproduced by applying the shallow potential in the coupled-channels calculations but that requires an additional weak absorption that acts near the minimum of the potential pocket. The calculated, high-energy cross sections are sensitive to the nuclear structure input parameters. By applying the structure input which has been extracted from inelastic scattering data it is possible to reproduce the high-energy data, even with a Woods-Saxon potential that has a normal diffuseness.

The energy dependence of the fusion cross section in the barrier region was also investigated. This region is best studied in terms of the extracted barrier distribution, which is usually very sensitive to the low-lying nuclear structure input in the coupled-channels calculations. The calculated barrier distribution for $^{48}\text{Ca}+^{96}\text{Zr}$ turned out to be very sensitive to multi-phonon excitations, in particular of the soft octupole node in ^{96}Zr . The best agreement with the measured barrier distribution was achieved by including excitations up to five phonons of this excitation mode. Unfortunately, the empirical knowledge of the nuclear structure at such high excita-

tion energies is poor and many other reaction channels may also affect the barrier distribution. It is therefore a serious challenge to theory to determine a credible nuclear structure input and explain the measured barrier distribution in detail.

Acknowledgments. We are grateful to A. Stefanini for many communications and for providing us with the data, and to B. B. Back, R. V. F. Janssens, and K. E. Rehm for a long-term collaboration on the subject of fusion hindrance. This work was supported by the U.S. Department of Energy, Office of Nuclear Physics, under Contract No. DE-AC02-06CH11357.

-
- [1] C. L. Jiang, B. B. Back, H. Esbensen, R. V. F. Janssens, and K. E. Rehm, Phys. Rev. **73**, 014613 (2006).
 - [2] J. O. Newton *et al.*, Phys. Lett. **B586**, 219 (2004).
 - [3] M. Dasgupta *et al.*, Phys. Rev. Lett. **99**, 192701 (2007).
 - [4] R. A. Broglia and Aa. Winther, *Heavy-ion Reactions*, Lecture Notes, Addison-Wesley (Redwood City CA, 1991).
 - [5] M. Evers *et al.*, Phys. Rev. C **78**, 034614 (2008).
 - [6] A. M. Stefanini *et al.*, Phys. Rev. C **73**, 034606 (2006).
 - [7] M. Trotta *et al.*, Nucl. Phys. **A787**, 134c (2007).
 - [8] S. Mişicu and H. Esbensen, Phys. Rev. C **75**, 034606 (2007).
 - [9] H. Esbensen and Ş. Mişicu, Phys. Rev. C **76**, 054609 (2007).
 - [10] H. Esbensen, Phys. Rev. C **77**, 054608 (2008).
 - [11] H. Esbensen and F. Videbæk, Phys. Rev. C **40**, 126 (1989).
 - [12] Evaluated Nuclear Data Structure Files (ENSDF), National Nucl. Data Center, Brookhaven Nat. Lab., <http://www.nndc.bnl.gov/>.
 - [13] N. Rowley, G. R. Satchler, and P. H. Stelson, Phys. Lett. B **254**, 25 (1991).
 - [14] H. Esbensen, Phys. Rev. C **72**, 054607 (2005).
 - [15] H. Timmers *et al.*, Nucl. Phys. **A633**, 421 (1998).
 - [16] A. M. Stefanini *et al.*, Phys. Rev. C **76**, 014610 (2007).
 - [17] C. L. Jiang *et al.*, Phys. Rev. Lett. **93**, 012701 (2004).
 - [18] C. L. Jiang, H. Esbensen, B. B. Back, R. V. F. Janssens, K. E. Rehm, Phys. Rev. C **69**, 014604 (2004).
 - [19] C. L. Jiang, K. E. Rehm, B. B. Back, and R. V. F. Janssens, Phys. Rev. C (in press).
 - [20] C. L. Jiang *et al.*, Phys. Rev. C **71**, 044613 (2005).